On the relation between the drag and lift coefficients and dynamic response of a low aspect ratio airfoil NACA0012 at low-to-moderate Reynold numbers

S. Martinez-Aranda,[1] A. L. Garcia-Gonzalez, L. Parras, C. del Pino, J. F. Velezquez-Navarro,

Fluids Mechanics Group, Department of Mechanical Engineering and Fluids Mechanics, University of Malaga, C/ Doctor Ortiz Ramos s/n, C.P. 29071 Malaga, Spain

Resumen

The influence of the angle of attack (AoA) and the chord Reynolds number (Re_c) on the lift and drag coefficients has been analyzed in a low aspect ratio NACA0012 airfoil. The experiments have been carried out in a relatively low turbulence wind tunnel with a digital force sensor. Results are shown for a range of airfoil chord Reynolds numbers $3.33 \cdot 10^4 \leq Re_c \leq 1.33 \cdot 10^5$ and angles of attack ranging from -35^o to $+35^o$. In addition, it has been studied the wing model dynamic response by means of a frequency analysis of the force temporal evolution. Thus, results show that wing-tip vortex causes a dramatic reduction of the lift coefficient. This tendency is smoother as Re_c increases. The profile stall appears between 12^o and 14^o in all cases. Universal fittings are proposed for any aspect ratio (AR) for C_{Dmin} and C_{Lmax}/C_{Dmin} comparing our experimental data and other researcher works. In addition, changes in the flow structures on the surface had been related to variations in the slopes of the lift coefficient curves $\Delta C_L/\Delta\alpha$ (namely as β_{L1} and β_{L2}). The dynamic analysis shows that the main response of the wing to the wind are the first two natural frequencies of wing-balance system. In addition, we found experimentally low and high frequency relevant vibrations related to the wing-tip vortex and the formation and emission of coherent turbulent structures, respectively. The wing vibration level depends on the flow characteristics on the surface and the wake profile behind the wing, so that, the Power Spectral Density (PSD) showed different tendencies depending on three AoA regions: $\alpha \leq \alpha_{stall}$, $\alpha_{stall} \leq \alpha \leq 20^o$ and $\alpha > 20^o$, together with the unpredictable effect of the Re_c.

Palabras clave: Finite wing, Low Re aerodynamics, Wing-tip vortex, Dynamic response, Fundamental vibration frequencies

1. Introduction

A wing profile is a surface that may be designed to provide the maximum lift force with the minimum drag. The relationship between both forces is mainly determined by the wing cross section aerodynamics features (Abbott and von Doenhoff, 1959).

[1]Corresponding author: E-mail: martinez.aa.ss@gmail.com Phone: +34 669591945

In finite wings at low-to-moderate Reynolds numbers, the drag and the lift coefficient variations at low-to-moderate Reynolds numbers are mainly due to three mechanisms: Wing-tip vortex [Mueller (1999); Mueller and Torres (2001)]; laminar boundary layer separation leading to the formation of a laminar separation bubble (LSB), transition to the turbulent shear layer and subsequent reattachment of the turbulent layer [Gad-el Hak (1990); Mueller (1985); Huang and Lee (1999)]; and the vortex shedding in the wake behind the wing [Huang and Lin (1995); Lee and Huang (1998); Huang and Lee (2000)]. Most of these investigations were performed analyzing only the flow behavior. But, the C_D and C_L experimental measurements involve a fluid-structure interaction, giving us an overview of the whole scenario between the wing and the flow that passes over it. For this reason, a dynamic response analysis of a low aspect ratio cantilever NACA 0012 profile is considered in this paper, besides of the C_D and C_L classical measurement in a wind-tunnel. The aim of this novel analysis is to study the possible relationships among wing-tip vortex, surface flow regimes, wake vortex and structural dynamic response.

The NACA 0012 airfoil has been extensively studied and its aerodynamics features are well-known. Abbott and von Doenhoff (1959) presented a large experimental data summary for different 2D airfoils. For NACA 0012 airfoil, the maximum C_L observed by Abbott was $1.1-1.6$ for chord Reynolds numbers between $3\cdot 10^6$ and $9\cdot 10^6$, with stall angles between 12^o and 16^o. For lower angles than the stall angle, the lift coefficient increases lineally with slope $\Delta C_L/\Delta\alpha \simeq 0.11 deg^{-1}$. The minimum C_D obtained by Abbott was $C_{Dmin} = 0.006-0.01$, depending on the roughness of the surface model.

Sheldahl and Klimas (1981) tested a 2D NACA 0012 model of 381 *mm* chord for chord Reynolds numbers between $3.6\cdot 10^5 \leq Re_c \leq 7\cdot 10^5$ and angles of attack (AoA) between $0^o < \alpha < 180^o$. Sheldhal results show reductions of the maximum lift coefficient ($C_{Lmax} = 0.9-1.0$) and of the stall angle ($\alpha_{stall} = 10^o - 12^o$). Although the lift curve slope for small AoA were in agreement with Abbott, this slope decreases when AoA was greater than $5^o - 6^o$. The drag coefficients obtained by Sheldahl were 0.008 and 0.028 for a null AoA and the stall angle, respectively.

However, if the geometric ratio chord/span of the wing (known as the aspect ratio, AR) falls down until reach a certain lower limit, three dimensional effects on the wing tip play a key role. This modifies the expected aerodynamics performance of the wing. Wing-tip vortex on finite wings generate a lift coefficient reduction respect to the 2D infinite airfoil as well as an increased of the drag coefficient. This behavior is even more significant if the aspect ratio reduces its value.

Laitone (1997) performed tests with a rectangular finite wing with a NACA 0012 profile of cross section, with AR=6, chord Reynolds numbers below $7\cdot 10^4$, and a free stream turbulence intensity $0.02\% - 0.1\%$. Laitone results showed a discontinuity in the slope on the lineal region of the lift curves for $Re_c = 2.07\cdot 10^4$ and $Re_c = 4.21\cdot 10^4$ and small AoA. This discontinuity decreases as the free stream velocity increases, together with the smooth increment of the slope $\Delta C_L/\Delta\alpha_0$. For a null AoA, the lift curve slope reported by Laitone was 0.041 for $Re_c = 2.07\cdot 10^4$ and 0.061 for $Re_c = 4.21\cdot 10^4$. The maximum lift coefficient for a constant Reynold

number was 0.455 for a free stream turbulence intensity 0.02% and 0.59 for a free stream turbulence intensity 0.1%, being 6^o and 8^o the stall angles respectively ($Re_c = 2.07 \cdot 10^4$).

Laitone reported a slightly reduction of the minimum drag coefficient C_{Dmin}, obtained for null AoA, with the increase of Re_c. The C_{Dmin} progression coincides with the expression $C_{Dmin} = 0.35 \cdot Re_c^{-0.25}$. The reported values of C_{Dmin} were 0.029 and 0.022, for $Re_c = 2.07 \cdot 10^4$ and $Re_c = 6.5 \cdot 10^4$, respectively.

Mueller (1999) performed experimental measurements of the drag and lift coefficients on wind tunnel for different wing models. These models had semi-span aspect ratios (*sAR*) between 0.5 and 3 and were built with a thin flat and chambered plates with rounded edges. The Reynolds numbers were constant between $6 \cdot 10^4$ and $2 \cdot 10^5$, and the AoA were varied between -15^o and $+25^o$. In addition, both flat and chambered 2D models were also studied. Mueller found a direct relationship between the wing aspect ratio and the drag and lift polars shape. Specifically, for a rectangular flat plate model, a *sAR* decrease from 3 to 0.5 caused a 50% reduction of C_L, for $\alpha = 10^o$ and $Re_c = 1.4 \cdot 10^5$. However, as the semi-aspect ratio was decreased, the linear region of the C_L vs α curve became longer and α_{stall} tended to increase. For the rectangular wing model with aspect ratio $AR = 2$ and a incident current of $Re_c = 1 \cdot 10^5$, Mueller and Torres (2001) obtained a $C_{Lmax} = 0.8$ for an stall angle of 18^o. The linear region slope of the lift curve ($\Delta C_L / \Delta\alpha$) was equal to 0.05 for small angles of attack. The C_{Dmin} was 0.04 for null lift position ($\alpha = 0^o$). Thus, the increase of the drag force due to the occurrence of edge effects (e.g. wing-tip vortex) was demonstrated.

Ngo and Barlow (2002) conducted measurements in a low turbulence wind tunnel of a rectangular NACA 0012 wing (146 mm chord, 559 mm length, $AR \approx 4$) in order to study a moving mechanism that allowed to reduce the drag force induced by the wing-tip vortex. The upstream flow Reynolds number was $Re_c = 4.8 \cdot 10^5$. Ngo and Barlow obtained a $C_{Dmin} = 0.048$ for $\alpha = 0^o$. The C_{Lmax} was around 0.6 for a stall angle $\alpha_{stall} = 11^o$.

Regarding to the study of the dynamic response analysis of wing models, to our knowledge there are no reported dynamic response data for a low aspect ratio NACA 0012 airfoils at low-to-moderate Reynolds numbers. It has been studied and reported the pitching oscillation of self-sustained NACA 0012 airfoils [Poirel et al. (2008); Kim and Chang (2013); Poirel and Yuan (2010)], but this oscillation analysis considerably differ from the dynamic response presented in this paper. Actually, the boundary conditions are completely different, for self-sustained airfoils it is need to attach both edges (so wing-tip vortex is neglected).

Rojratsirikul et al. (2010) and Rojratsirikul et al. (2011) have reported experimental modal analysis for low aspect ratio rectangular membrane wings. The modal analysis was performed by means of Digital Image Correlation (DIC) technique, so in this case deformation data were reported and no forces were measured. This analysis was performed in order to find relations among the wing deformations and the flow, and Rojratsirikul et al. (2010) literally suggested a possible coupling between the membrane vibration with the wake instabilities for all airfoils. To shed some new light into this, we have analyzed in this work the dynamic response, despite of the stiffness differences between elastic membranes and the rigid aluminum NACA 0012 profile, used in this paper.

2. Experimental Setup

Experimental tests were performed in the Vehicles Aero-Hydrodynamics Laboratory closed low-speed wind tunnel, which has a 5 m long closed test section, with a squared cross-section of 1 m^2. The free-stream velocity ranging from $U_\infty = 4\ m/s$ to $U_\infty = 30\ m/s$. The turbulence level (Turbulence Intensity I $[\%]$) is shown in the Table 1 below.

The tested model was a solid rectangular wing NACA 0012 airfoil. The wing model is 100 mm chord and 200 mm length ($AR = 2$) and was made of an aluminum alloy. The model maximum thickness was 12 mm at 30 mm from the profile leading edge (Del Pino et al., 2011).

The wing was firmly fixed to a base, also made of aluminum, allowing coupling the wing to a precision force sensor placed below the test section floor. This device is capable of measuring forces and moments in all three spatial orthogonal dimensions and was leveled in that way its Z axis coincided with the vertical to the measurement section floor (Figure 1). The $X-Y$ balance plane was perpendicular to the longitudinal axis of the wing.

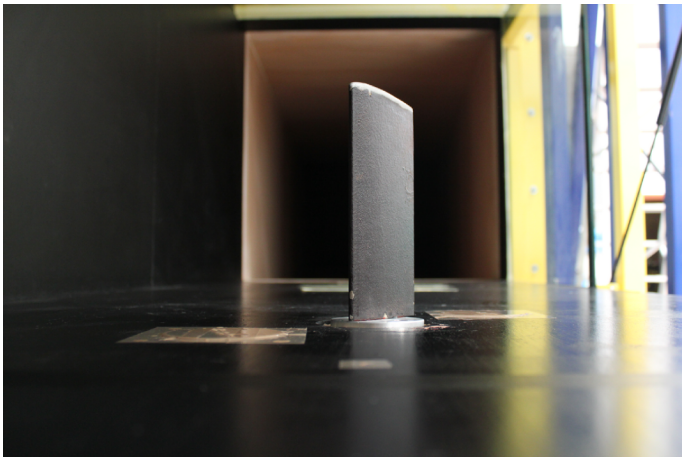

Figure 1: NACA 0012 model mounted in the wind tunnel.

The balance was coupled to an automatic rotation system which allows to vary the wing-base-balance system orientation in the range of $\alpha_r = [-180^o, 180^o]$ (Figure 2).

The forces in each orthogonal direction were recorded as voltage data in a range of $0\ V \leq V_{output} \leq 5\ V$, with a sampling frequency of $f_s = 250\ points/sec$,. For this equipment the conversion factor between measured force and electrical output is $K = 32N/5V$.

The rotation system was calibrated in order to find the zero angle $\alpha = 0^o$ where the lift force is equal to zero and the drag force presents minimum value. Therefore, series of tests were conducted for AoA between $-10^o \leq \alpha_r \leq +10^o$ in order to detect the symmetry axis of the graph $F = \sqrt{F_x^2 + F_y^2}$ vs α_r, that corresponded with the α_r where the force F presented the minimal value.

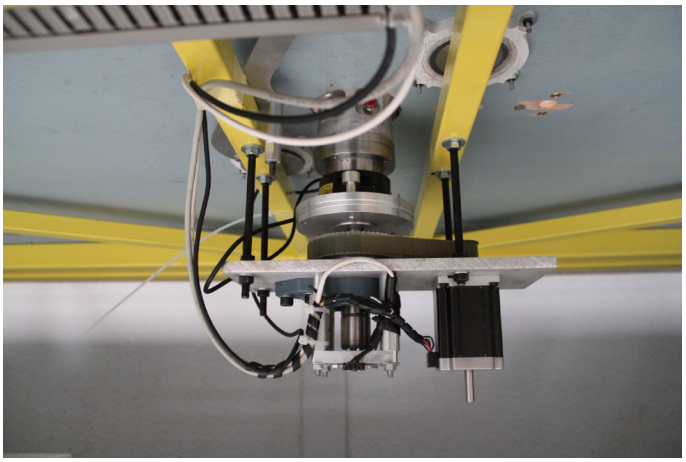

Figure 2: Precision 3D scale and automatic system of rotation.

Experiments were carried during $T = 200s$ for AoA's ranging from $\alpha = -35^o$ to $\alpha = +35^o$ in increments of 1^o or 2^o, depending on the case. On the other hand, the free-stream velocity U_∞ was calibrated by means of *Laser Doppler Anemometry* (LDA). The percentage of power $\%P$ applied to the four wind-tunnel fans (relative to their nominal power) was the dependent parameter. The values $\%P$, $U_{\infty LDA}$ y $\delta U_{\infty LDA}$ were previously tabulated. Tests were performed for four different free stream velocities U_∞. The chord Reynolds number Re_c is defined as $Re = U_\infty \cdot c \cdot \nu^{-1}$, being c the chord ($c = 100\ mm$) and ν the kinematic viscosity of the air (see Table 1).

Before proceeding a set of experiments for different AoA and a constant value of the Reynolds number, several measurements were carried out without velocity in the tunnel in order to determine the *offset* (F_{x0}, F_{y0}) for the value of the force in the plane $X - Y$, and possible Z axis scales deviations from vertical axis and the weight of the wing. Then, tests were carried out continuously, acquiring the air temperature inside the tunnel for each experiment. Fluctuations in the air temperature were within 0.2^oK for a single test. The dynamic strength have been calculated with an air density adjusted depending on the temperature of the performed test.

Once experimental tests were finished, X and Y axis force data were processed using a *Matlab* code. The drag C_D and lift C_L coefficients values were calculated for each AoA and Reynolds number. C_D and C_L are experimental coefficients, being the same experimental procedure repeated three times and computing the average value. The standard deviation will be discussed below. As it is shown in equation (1) and (2), due to the fact that the balance system is rotating mutually to the automatic rotation system, the measurement axis system of the balance changes for each angle, so to obtain the lift and drag forces, the measured forces must to be projected onto the axis of the tunnel. The parameters, angles, forces and coefficients that appear in this study are:

$$\alpha_{axis} = \alpha_{dev} + \alpha$$

$$F_{x\ net} = F_x - F_{x0} \qquad F_{y\ net} = F_y - F_{y0}$$

$$D = F_{x\ net} \cdot cos(\alpha_{axis}) + F_{y\ net} \cdot sin(\alpha_{axis}) \tag{1}$$

$$L = -F_{x\ net} \cdot sin(\alpha_{axis}) + F_{y\ net} \cdot cos(\alpha_{axis}) \tag{2}$$

$$C_D = \frac{D}{\frac{1}{2}\rho\, U_\infty^2\, A} \qquad C_L = \frac{L}{\frac{1}{2}\rho\, U_\infty^2\, A}$$

where the different symbols are:

α : NACA 0012 model angle of attack (AoA);

α_{dev} : Angle between the X balance axis and the null AoA;

α_{axis} : Angle between the X balance axis and the drag direction;

F_x, F_y : X and Y axis forces;

F_{x0}, F_{y0} : *offset* of X and Y axis forces;

$F_{x\ neta}, F_{y\ neta}$: X and Y axis net forces;

D, L : Drag and lift forces on the model;

C_D, C_L : Drag and Lift coefficients;

ρ : Air density inside the wind tunnel;

U_∞ : Free stream velocity;

$A = L \cdot c$: Aerodynamic area of the rectangular model (span x chord);

Re_c : Chord Reynolds number;

ν : Kinematic viscosity of the air;

3. Results and Discussion

3.1. Drag and Lift Curves

The drag and lift coefficients obtained in this work (Figure 3 and 5) differ quantitatively from those provided by Abbott and von Doenhoff (1959) and Sheldahl and Klimas (1981) for a 2D NACA 0012 airfoil. Although

the experiments were developed with different Re_c (especially compared to Abbott and von Doenhoff results), the main cause of this divergence is the appearance of effects in the trailing edge downstream the wing or wing-tip vortex, which dominate the wing aerodynamic performance due to the low aspect ratio of the model used ($AR = 2$).

The drag coefficient induced by the three-dimensional flow in the wing tip vortex at zero degrees was approximately six times greater than the C_{Dmin} for a 2D profile observed by Sheldahl. In addition, there is a delay around 2^o for the stall angle. The minimum drag coefficient C_{Dmin} at zero AoA ($\alpha = 0^o$) was between 0.053 and 0.072 in all cases. These values show a slight deviation compared to those published by Ngo and Barlow (2002). The differences between them were less than 15% for drag coefficients at AoA lower than the stall angle. As expected, the stall angles obtained were slightly higher than those reported by Ngo, due to the aspect ratio reduction. Similarly, the values of C_{Dmin} obtained are in agreement with those obtained by Mueller and Torres (2001) for a flat wing with the same aspect ratio and Reynolds numbers. Regarding drag coefficient slope, when stall angle was reached, between 12^o and 14^o, the slope $\Delta C_D/\Delta\alpha$ increases and the wing loses its aerodynamic effectiveness. Each case had a different slope, being very small for lower angles in comparison to the stall ones.

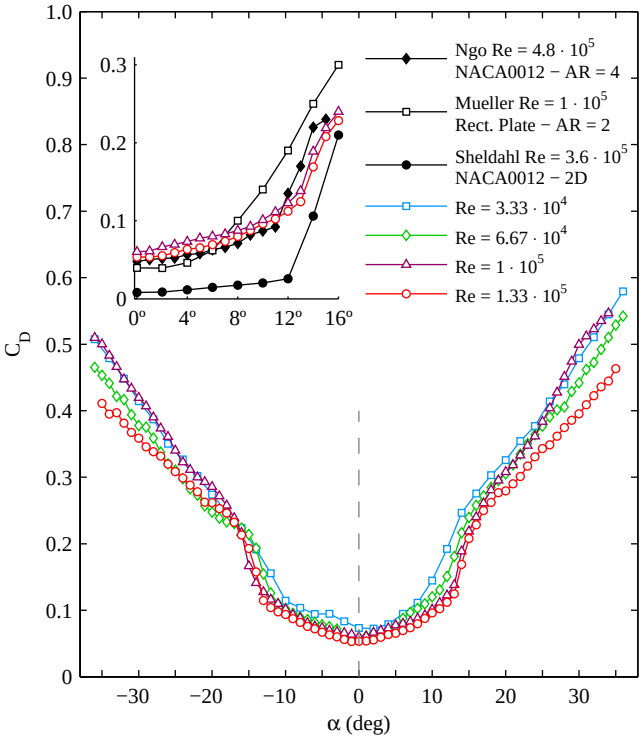

Figure 3: C_D vs α with a detail for high Reynolds numbers, together with those reported by Ngo and Barlow (2002), Mueller and Torres (2001) and Sheldahl and Klimas (1981).

The minimum drag coefficient had a decrease as the Re_c was increased (Figure 4). The experimental points

can be adjusted using the following equation $C_{Dmin} = 0.55 \cdot Re_c^{-0.21}$ [Figure 4 (a)]. Laitone (1997) obtained the equation $C_{Dmin} = 0.35 \cdot Re_c^{-0.25}$ to fit the minimum drag coefficient in cases with $2 \cdot 10^4 \leq Re_c \leq 7 \cdot 10^4$. The main cause of this difference, especially in the range of C_{Dmin}, are the different aspect ratio used in both experiments and the different Reynolds numbers tested. Nevertheless, we suggest an universal fitting using the law for any AR: $CD_{min} \cdot AR = 2 \cdot Re_c^{-0.25}$ [see figure 4 (b)]. On the one hand, there is a good agreement for the data reported by Laitone (1997) and Sheldahl and Klimas (1981) for different AR and Re_c. On the other hand, there is a disagreement with those results reported by Ngo and Barlow (2002) and Yen and Huang (2009). These discrepancies could be explained in terms of edge effects, surface roughness, the minimum offset used in the force sensor or the turbulence intensity in the wind tunnel.

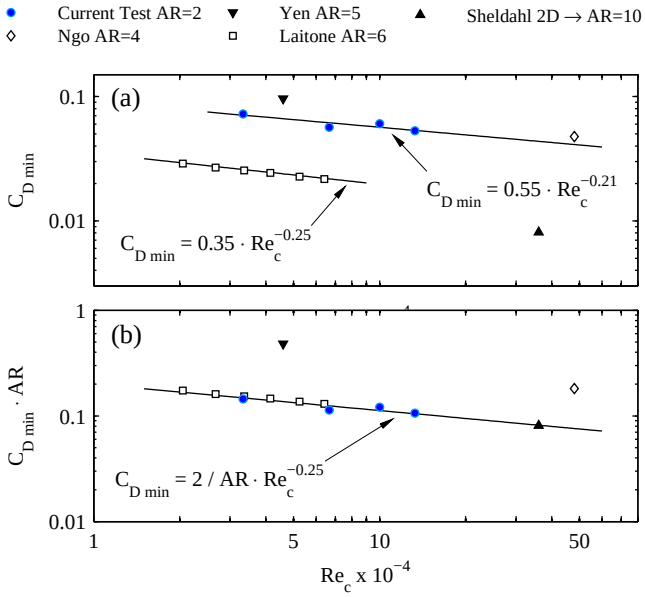

Figure 4: (a) C_{Dmin} vs Re_c for $3.33 \cdot 10^4 \leq Re_c \leq 1.33 \cdot 10^5$ and $AR = 2$ compared with the results of Ngo and Barlow (2002), Yen and Huang (2009), Laitone (1997) and Sheldahl and Klimas (1981). (b) $CD_{min} \cdot AR$ vs Re_c for the universal fitting law $CD_{min} = 2/AR \cdot Re_c^{-0.25}$.

Regarding the lift coefficient (Figure 5), the maximum lift coefficient C_{Lmax} reduction was about 40% for the tested model compared to the values observed by Sheldahl. The maximum lift coefficient C_{Lmax} was between 0.52 and 0.61 for all tested Reynolds numbers, and the stall angles α_{stall} were between 12 and 14 degrees. These values show a slight deviation compared to those published by Ngo and Barlow (2002). The values of C_L obtained are in agreement with those obtained by Mueller and Torres (2001) for a flat wing with the same aspect ratio and Reynolds numbers.

The slopes of the lift coefficient curves $\Delta C_L/\Delta\alpha$ were defined as β_L (Figure 5 and 6). Another ranging discrimination has been proposed attending to the relation between β_L and AoA. The slopes for null angle of attack and for AoA between $5^o - 6^o$ and $10^o - 11^o$ are β_{L1} and β_{L2}, respectively. These slopes define two linear regions of the lift curve whose tendencies were analyzed. β_{L1} and β_{L2} for higher Reynolds numbers were plotted

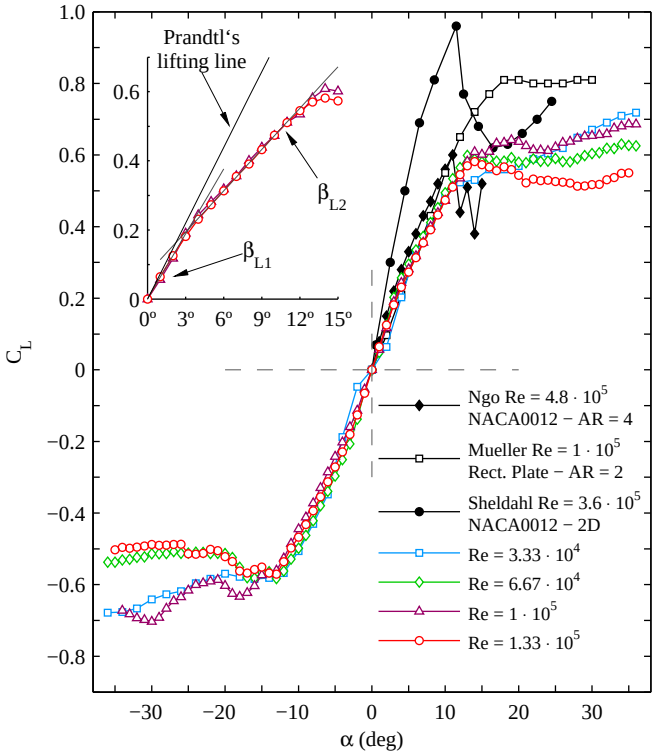

Figure 5: C_L vs α with a detail for high Reynolds numbers, together with those reported by Ngo and Barlow (2002), Mueller and Torres (2001) and Sheldahl and Klimas (1981). Detail: β_{L1} and β_{L2} for higher Reynolds numbers compared to the result from Prandtls lifting line theory for symmetric, rectangular wing with no twist and finite span Keuthe and Chow (1997).

in the inset Figure 5 together to the results from Prandtls lifting line theory for symmetric, rectangular wing with no twist and finite span, $C_L \approx m\alpha$ with $m = 2\pi/(1+1/(sAR))$, [see Keuthe and Chow (1997)]

For the two lowest Reynolds numbers tested, the linear region of the lift curve (before stall) has a discontinuity at small AoA (see Figure 6). For the region of low lift, the curve slope β_{L1} were 0.032 deg^{-1} and 0.048 deg^{-1} for $Re_c = 3.33 \cdot 10^4$ and $6.67 \cdot 10^4$, respectively. On the one hand, these slopes are significantly lower than those reported by Laitone (1997) for similar Re_c, in a NACA 0012 wing with $AR = 6$ and AoA close to zero. On the other hand, the lift coefficients curves show a similar behavior to those achieved by Laitone as the free stream velocity U_∞ was increased, the discontinuity of slope β_{L1} was smoothly reduced, so the final tendency was a constant slope at small AoA ($0^o \leq \alpha \leq 3^o$).

The slopes β_{L1} for high Reynolds numbers were $0.059\,\mathrm{deg}^{-1}$ and $0.063\,\mathrm{deg}^{-1}$ for $Re_c = 1 \cdot 10^5$ and $Re_c = 1.33 \cdot 10^5$ respectively. These slopes at the origin were far from those reported by Sheldahl and Klimas (1981) for a 2D model and Re_c of the same order of magnitude ($\beta_{L1} = 0.11\ deg^{-1}$). However they are practically in agreement with the data for small AoA by Mueller and Torres (2001) for a flat plate with $AR = 2$ ($\beta_{L1} = 0.05\ deg^{-1}$) and with those obtained by Ngo and Barlow (2002) for the NACA 0012 with $AR = 4$ ($\beta_{L1} = 0.075\ deg^{-1}$).

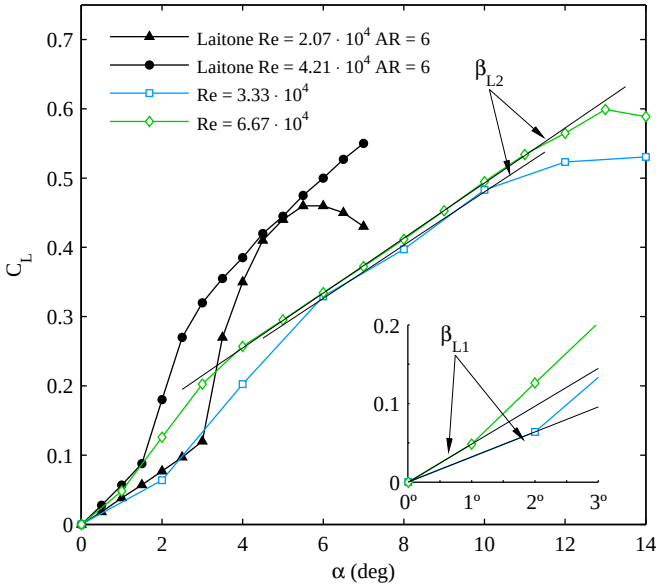

Figure 6: C_L vs α for $Re_c = 3.33 \cdot 10^4$ and $Re_c = 6.67 \cdot 10^4$ with AoA values lower than the stall angle ($AR = 2$), together with Laitone's data ($AR = 6$, $I = 0.02\%$).

We suggest another universal fitting for β_{L1} and β_{L2} for any AR [see Figure 7 (a) and (b)]. For $Re_c < 1.5 \cdot 10^5$, $\beta_{L1} \cdot AR^{-0.5} = -2 \cdot 10^{-}12 \cdot Re^2 + 5.5 \cdot 10^{-}7 \cdot Re + 0.0064$; for $Re_c > 1.5 \cdot 10^5$, $\beta_{L1} \cdot AR^{-0.5} = 1 \cdot 10^{-}8 \cdot Re + 0.034$; for any Re_c, $\beta_{L2} \cdot AR^{-0.5} = 8 \cdot 10^{-}9 \cdot Re + 0.027$. Regarding to $\beta_{L1} \cdot AR^{-0.5}$, there was an excellent agreement for the cases with similar Re_c reported by Laitone (1997) and Yen and Huang (2009). $\beta_{L1} \cdot AR^{-0.5}$ was strongly dependent on Re_c for $Re_c \leq 1 \cdot 10^5$, but for higher Re_c, the $\beta_{L1} \cdot AR^{-0.5}$ tendency changed to remain constant with Re_c variation. This change in the tendency was in agreement with data reported by Ngo and Barlow (2002) and Sheldahl and Klimas (1981) for higher Re_c. Regarding to $\beta_{L2} \cdot AR^{-0.5}$, there is a reasonable good agreement with all data reported. $\beta_{L2} \cdot AR^{-0.5}$ is almost independent of Re_c.

Finally, the maximum lift coefficient C_{Lmax} was plotted against Reynolds number Re_c [see Figure 7 (c)]. For low Reynolds number, the C_{Lmax} increased as Re_c. But, once Re_c is higher than $1 \cdot 10^5$, all data collapsed around 0.6, so C_{Lmax} was independent of Re_c for $Re_c > 1 \cdot 10^5$. This fact was consistent with the results provided by McArthur (2008).

The maximum efficiency AoA is found in the polar curve between 10^o and 12^o, depending on the incident flow velocity (see Figure 8), being the ratio C_L/C_D between 4,43 for $Re_c = 3.33 \cdot 10^4$ and 5,51 for $Re_c = 1 \cdot 10^5$. There is a slight increase in the efficiency with the Reynolds number. This fact is due to lower drag coefficients and the increment of the lift coefficient at small AoA.

C_{Lmax}/C_{Dmin} was plotted against Re_c [see Figure 9 (a)] for all the Reynolds number tested compared to those provided by Ngo and Barlow (2002), Yen and Huang (2009), Laitone (1997) and Sheldahl and Klimas (1981). Then, we suggest an universal fitting using the law for any AR: $C_{Lmax}/C_{Dmin} = 0.27 \cdot AR \cdot Re_c^{0.25}$. There is again

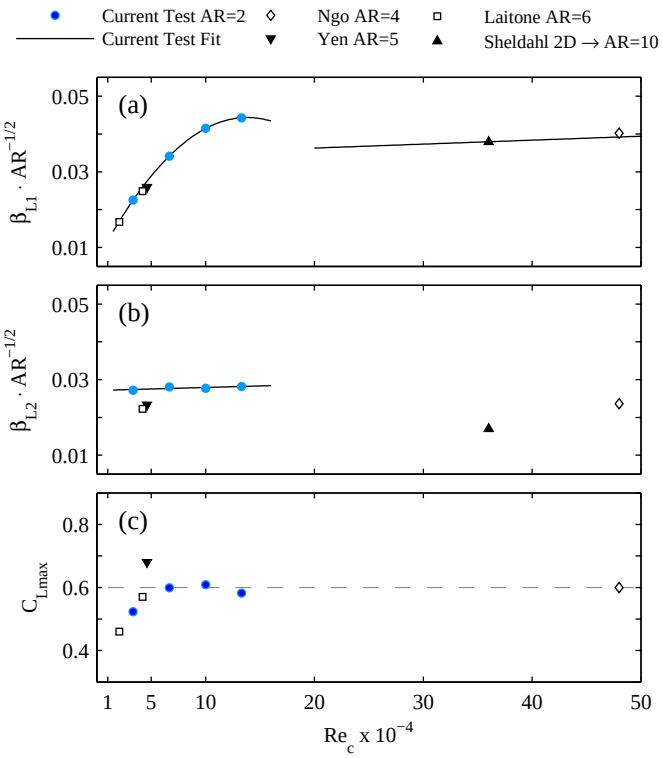

Figure 7: (a) Universal fitting for $\beta_{L1} \cdot AR^{-0.5}$ vs Re_c for $3.33 \cdot 10^4 \leq Re_c \leq 1.33 \cdot 10^5$ and $AR = 2$ compared with the results of Ngo and Barlow (2002), Yen and Huang (2009), Laitone (1997) and Sheldahl and Klimas (1981). (b) Universal fitting for $\beta_{L2} \cdot AR^{-0.5}$ vs Re_c. (c) C_{Lmax} vs Re_c for $3.33 \cdot 10^4 \leq Re_c \leq 1.33 \cdot 10^5$ and $AR = 2$ compared with the results of Ngo and Barlow (2002), Yen and Huang (2009) and Laitone (1997).

an excellent agreement for the data reported by Laitone (1997).

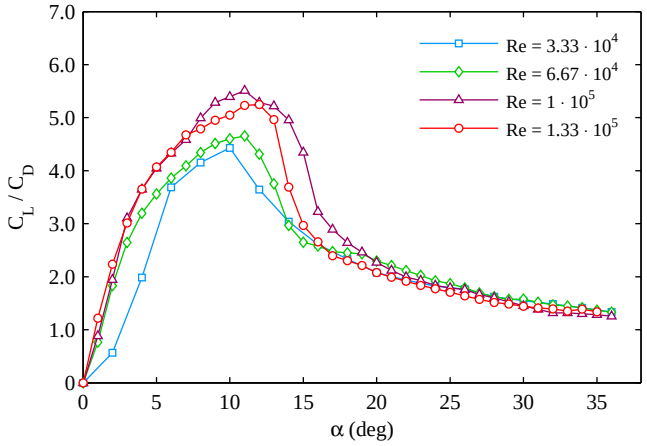

Figure 8: C_L/C_D vs α for all Reynolds numbers tested.

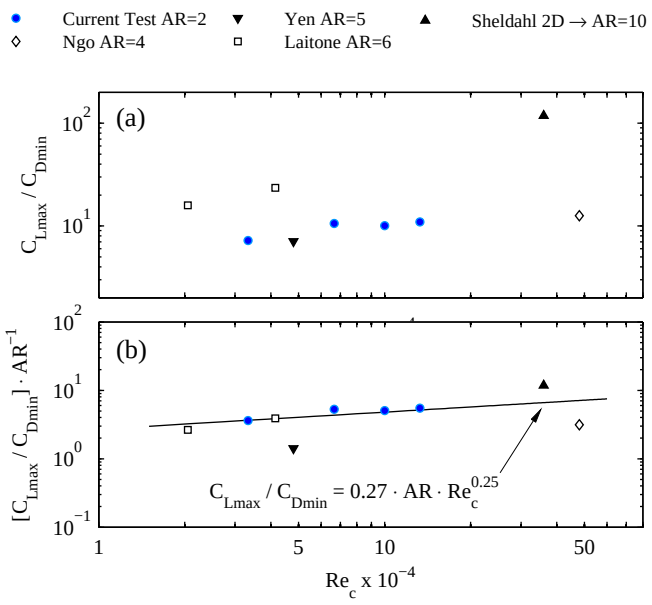

Figure 9: (a) C_{Lmax}/C_{Dmin} vs Re_c for $3.33 \cdot 10^4 \leq Re_c \leq 1.33 \cdot 10^5$ and $AR = 2$ compared with the results of Ngo and Barlow (2002), Yen and Huang (2009), Laitone (1997) and Sheldahl and Klimas (1981). (b) $C_{Lmax}/C_{Dmin} \cdot AR^{-1}$ versus Re_c for the universal fitting law: $C_{Lmax}/C_{Dmin} = 0.27 \cdot AR \cdot Re_c^{0.25}$.

3.2. Coefficient deviations and errors

Figure 10 (a) shows the deviations for AoA between $\alpha = 0^o - 35^o$ and Reynolds numbers $Re_c = 1.33 \cdot 10^5$, which is the unfavorable case. The other cases analyzed in this work show a similar behavior. The standard deviation of the force data for each Reynolds number and AoA introduced fluctuations on the calculated (average) drag and lift coefficients. The coefficients deviation remains practically constant until the stall angles ($\alpha \leq 12^o - 14^o$) and these variation were around 0.025 for both C_L and C_D in all Reynolds numbers tested. Observed absolute deviations of the coefficients with AoA smaller than 12^o remained basically constant for all Reynolds numbers tested [Figure 10 (b)].

For angles equal or slightly higher than the stall ones, vortex were generated in the boundary layer separated from the profile surface. This vortex moved downstream as a turbulent wake, and it induced a greater fluctuation in the forces measurement, resulting a sudden increase of the coefficients deviations C_L and C_D. The maximum deviations were shown for AoA between 12^o and 20^o in all cases, and their values were always less than 0.135 (15% *aprox.*) for both, C_D and C_L. The coefficient deviations gradually drop when angles of attack are greater than 20^o [Figure 10 (b)]. The vortex generation in the separated turbulent boundary layer induced a shrinking wing vibration and consequently, the variations in the force amplitude were reduced.

The Kline and McClintock (1953) method has been used to calculate the propagation of experimental errors in the measurements, so one can estimate the accuracy of the aerodynamic coefficients. Considering the formulation used to determinate the coefficients, this method yields the highest error for AoA α_{axis} close

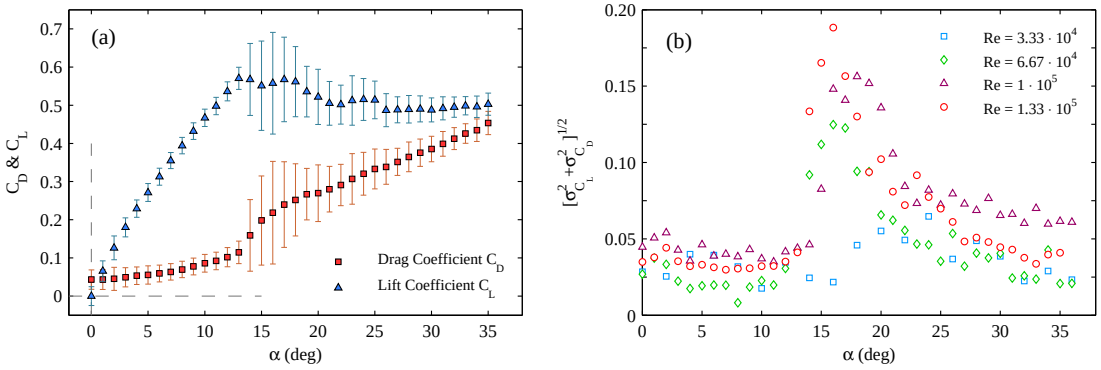

Figure 10: (a) C_D y C_L deviations for $Re_c = 1.33 \cdot 10^5$ and (b) absolute deviations of the coefficients for all AoA and Reynolds numbers tested.

to zero. The accuracy of the measured force (N) was $0,2\%$, the rotational accuracy of the system was 0.2^o and velocity variations were above considered (see Section 2). The estimated maximum errors for each test Reynolds number are shown in Table 2, showing a good experimental procedure in the computation of the coefficients.

3.3. Wing vibrations and discussion

The temporal evolution of raw force acting on the wing has been analyzed for all AoA and Reynolds numbers tested. Then, the power spectral density (PSD) for each signal in frequency domain has been calculated by the *Matlab* in-built FFT function. The force results are subtracted by their mean values, so we studied the time variation and energy of the variation of the force.

As it was stated above, the sampling frequency of the scales was $f_s = 250\ Hz$, the time recording of the tests was $T = 200\ seg$, so the frequency resolution was $df = 0,005\ Hz$. In order to avoid aliasing effects in the digital signal, this was previously filtered by a low pass filter which removed the components with frequencies above the Nyquist one ($F_{Nyquist} = f_s/2$).

The wing dynamic response due to the wind action depends essentially on the structural features of the model. For this reason, the natural frequencies of the wing model fixed to the force sensor was obtained experimentally by two sets of ten tests with no velocity inside the wind tunnel. The first testing consisted of an instant impact at the free end wing center in a perpendicular direction to the chord. Thus, the model vibrates freely and the net force on the scale was recorded. The temporal signal was analyzed by means of the FFT function (Figure 11). A main natural vibration frequency was detected at $f_{1st} \approx 28.25\ Hz$. The second testing consisted of an instant impact at the cylindrical aluminum base which fixed the wing to the force sensor. The main vibration frequency f_{1st} was also detected in all tests. However, a second main vibration frequency appears at $f_{2nd} \approx 43.50\ Hz$ (Figure 12). Therefore, f_{1st} and f_{2nd} are the first and the second natural mechanic frequencies of the wing-base-force sensor system.

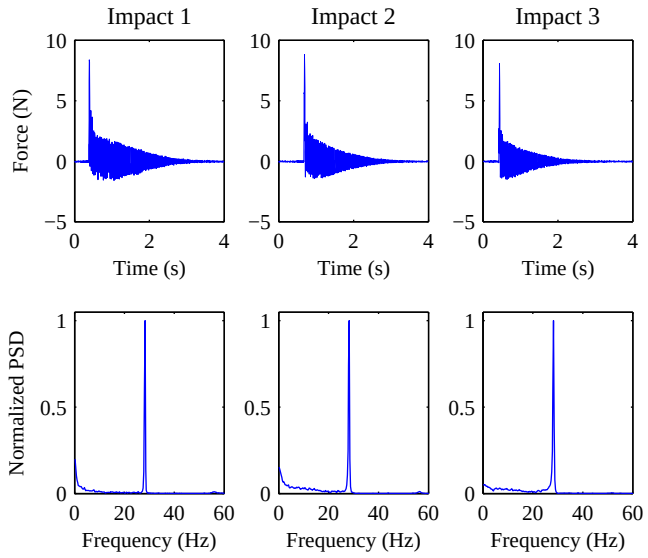

Figure 11: Net force vs time and power spectral density (PSD) for three impacts at the free end wing. The main vibration frequency of the system was 28.25 Hz in all impact tests.

The natural vibration frequencies for a rectangular aluminum plate were experimentally obtained by Dalley and Ripperger (1954). The rectangular plate had an aspect ratio $AR = 2$, perfectly embedded in one of its short edges and free at the other. Dalley observed a frequency parameter value for the first natural mode $\lambda = \omega \cdot a^2 \cdot \sqrt{\rho/D} = 3.36$, where ω is the first mode frequency, a the length of the plate, ρ material density and $D = \dfrac{E \cdot h^3}{12 \cdot (1-\nu^2)}$ the bending modulus of the plate (E is the material Young modulus, h the plate thickness and ν the Poisson module). An equivalent rectangular solid plate has been considered with the same moment of inertia I, same cross-sectional area a_t and same aspect ratio AR that the tested NACA 0012 airfoil. This frequency parameter is equivalent to a free vibration frequency in the first mode of 29.43 Hz, very close to that obtained experimentally for our model.

In addition, the frequencies of the first three natural vibration modes of the equivalent plate have also been calculated analytically by means of the formulation developed by Warburton (1954). Warburton formulation is based on Rayleigh method and matching deflection functions on the plate to the product of blending deformation functions in beams with the same boundary conditions and orthogonal directions. For a rectangular solid aluminum plate with same mechanical characteristics as the NACA 0012 airfoil tested (I, a_t, AR and material), the first natural frequency for the first symmetric deformation mode was 30.81 Hz. This first mode has the smallest characteristic frequency and requires less input energy to produce than anyone. The frequencies obtained for the second and the third natural vibration modes are 154.56 Hz and 192.97 Hz, respectively.

The theoretical values of the first natural frequency for the low aspect ratio plate was in agreement with

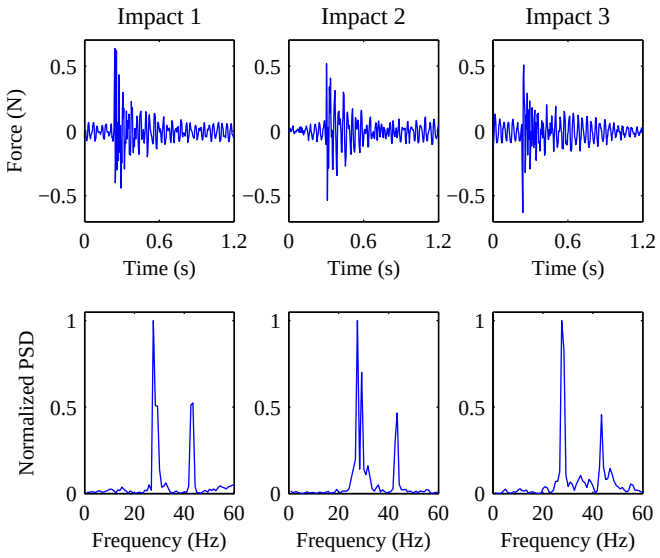

Figure 12: Net force vs time and power spectral density (PSD) for three impacts at the cilindrical base. The second main vibration frequency of the system was 43.50 Hz in all impact tests.

experimental data obtained for our wing model by the impact tests. The small differences between theoretical and experimental data on this first natural frequency may be primarily due to the difference among real and theoretical boundary conditions; and secondly, the difference between NACA 0012 profile and its equivalent rectangular plate.

As was expected, the net aerodynamic force signal has an important sinusoidal component with the two first natural frequencies in all cases. The first frequency vibration was almost independent of the behavior of the flow around the model. The second natural frequency vibration, that is less dominant than the first one, was affected by the possible aerodynamic interactions. Figures 13 (a), (b), (c) and (d) represent the spectral density, scaled according to their magnitude order, of the net force on the wing for AoA between 0^o and 30^o and all tested Reynolds numbers. All responses have a high energy peak at the two first natural frequencies of the wing-base-scale system ($f_{1st} \approx 28.25Hz$ and $f_{2st} \approx 43.50\ Hz$).

Nevertheless, the energy involved in the vibration (amplitude of force fluctuation) depends on the flow characteristics, especially the vortex emission and propagation in a turbulent separation boundary layer from the NACA0012 airfoil. The energy force spectrum was more than an order of magnitude higher for AoA slightly greater than stall ones ($12^o - 14^o \leq \alpha \leq 20^o$) than for angles $\alpha < 12^o - 14^o$. As the AoA was increased below 20^o, the spectral density decreases again. However, the spectral density was higher for AoA below 20^o than for smaller angles to the stall ones.

This sudden increment of the energy for stall angles was specially important at small frequencies. For frequencies between $0.1\ Hz \leq f \leq 3\ Hz$ the sudden increment of the energy involved in vibration for

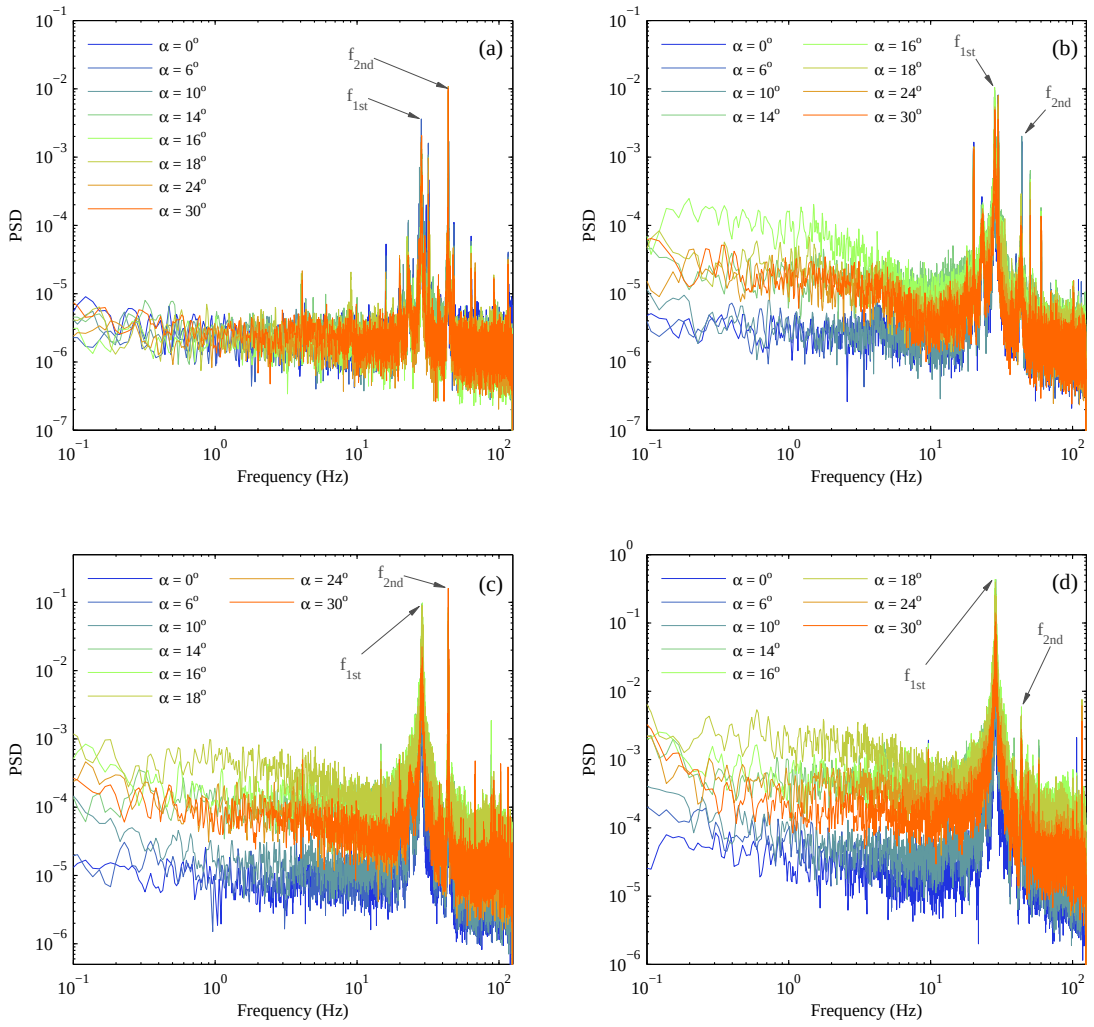

Figure 13: PSD of the net force signal for (a) $Re_c = 3.33 \cdot 10^4$, (b) $Re_c = 6.67 \cdot 10^4$, (c) $Re_c = 1 \cdot 10^5$ and (d) $Re_c = 1.33 \cdot 10^5$, and angles of attack between 0^0 to 30^o.

$14^o \leq \alpha \leq 20^o$ could be two order of magnitude higher than for AoA previous to the stall ones [see Figures 13 (b), (c) and (d)].

Similarly, the magnitude of the forces spectral density increases at all AoA more than two orders of magnitude as the incident flow velocity increases from $Re_c = 3.33 \cdot 10^4$ to $Re_c = 1.33 \cdot 10^5$. Figure 14 shows the net force PSD spectra for several angles of attack (small angle $\alpha = 6^o$, stall angle $\alpha = 18^o$ and high angle $\alpha = 30^o$) and for all the Re_c tested . This behavior may be simply due to an increase of the turbulent kinetic energy transported by increasing the value of the free stream velocity. However, it could be observed that, for stall AoA ($\alpha = 18^o$), the energy increment with Re_c is greater than for those AoA different to the stall ones.

The distribution of the PSD as a function of the AoA was directly related to the observed deviation in the

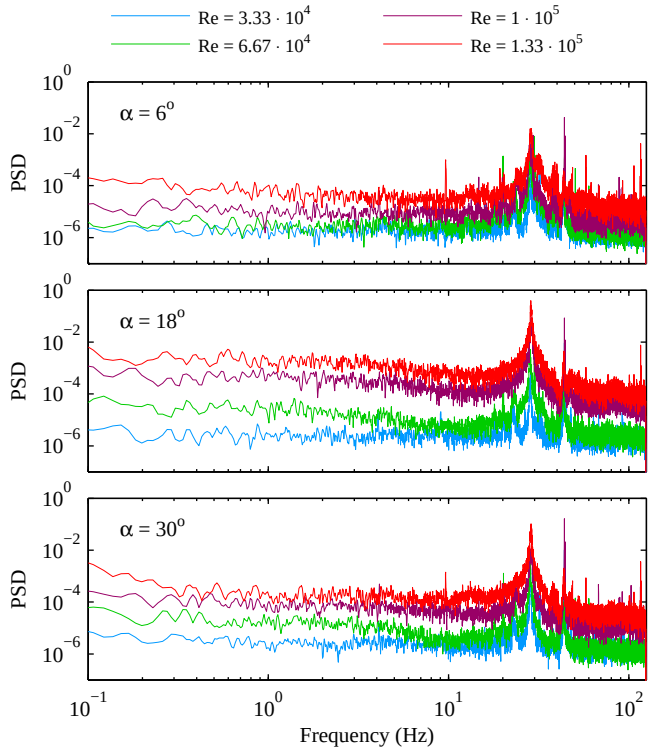

Figure 14: PSD of the net force signal for all Re_c cases and angles of attack $\alpha = 6^o$, $\alpha = 18^o$ and $\alpha = 30^o$.

coefficients C_D and C_L. An increasing vibration energy for AoA equal or slightly higher than the stall ones was always present for the three highest Reynolds numbers tested. The standard deviation of the coefficients also increased for these angles [Figure 10 (b)]. However the increment of energy for angles in the range $12^o \leq \alpha \leq 20^o$ tends to be small, so the standard deviation, as Re_c decreases. Figure 13 (a) shows the PSD is equal in magnitude for all the AoA and $Re_c = 3.33 \cdot 10^4$. As it was expected, the standard deviations of aerodynamic force on the wing model were approximately equal for all AoA in this case.

The energy increment at AoA stall angles was mainly due to variations in the excitation characteristics, changes in the frequency and scale of coherent turbulent structures formed on the surface and on the trailing wake behind the wing. Yarusevych et al. (2009) found that, for a NACA 0025 (another wing platform with symmetrical airfoil section), the fundamental frequency of shear-layer disturbances in the laminar separation without reattachment regime varied slightly respect to the changes in the angle of attack (0^o, 5^o, and 10^o) for Reynolds numbers of 10^4. This fundamental frequency increased at the same time with Re_c, but it had the same order of magnitude of $10^1 Hz$ for all AoA. This increment of the fundamental shear-layer frequency disturbances with Re_c was also observed by Huang and Lin (1995) for a NACA 0012 airfoil, confirming our results.

Yarusevych et al. (2009) observed that if the Reynolds number Re was increased over 10^5, the turbulent boundary layer would reattached to the surface and it created a flow separation bubble on the surface flow. The

global frequency triggered by turbulent structures were consistent with this bubble pulsation ($10^2 - 10^3\ Hz$) and it depends on the AoA. These structures, generated in the shear-layer separation bubble, interact in the turbulent wake creating larger scale vortex for smaller Re_c and spread frequencies of an order of magnitude lower than fundamental frequency of the shear-layer disturbances (measured at a $x/c \leq 2$ distance of the trailing edge). Vortex shedding frequency behind a NACA 0012 airfoil was also measured by Lee and Huang (1998). For small angles of attack ($0^o \leq \alpha \leq 5.5^o$) and $Re_c = O(10^4)$, Lee and Huang (1998) observed that the shedding frequencies in the wake increases with Re_c and they decreased as the AoA increased (subcritical regime).

For high AoA, the separation bubble becomes more long-lasting and moves towards the leading edge, until it produces a new separation of the turbulent boundary layer profile (bubble burst) and stalls for $\alpha = 12^o - 14^o$. For these angles of attack, there was a sharp drop in the fundamental frequency (f_0) of the disturbances in the separated turbulent boundary layer, as it was reported by Gerakopulos (2011) for a NACA 0018 airfoil. The higher the Re_c was, the more pronounced the f_0 dropped. Lee and Huang (1998) reported that, for AoA higher than stall one, vortex shedding frequency in the wake slighly decreased and increased with the AoA and the Re_c, respectively. This fact was also observed by Yen and Huang (2011), for a NACA 0012 swept-back finite wing for Re_c close to 10^4, with AoA below $\alpha = 22^o$ (turbulent separation regime).

Regarding to our results, the PSD increment might be related to the frequency drop in the vortex shedding flow separation that occurs for the stall AoA and all Re_c. As we stated above, this change in the emission frequency was more pronounced at high Reynolds number. Therefore, the drag and lift forces fluctuations are increased when the profile stalls. For lower AoA than the bubble burst ones and for higher AoA than stall ones, the frequencies vary slightly, so that, the force variations were also small.

In order to summarize this PSD dependence on the Re_c and AoA, we suggested three ranges of Re_c and AoA (see Table 3). Regarding to AoA, the PSD tendency could be summarized for $\alpha \leq \alpha_{stall}$, $\alpha_{stall} \leq \alpha \leq 20^o$ and $\alpha > 20^o$. Regarding to Re_c, the three ranges were $Re_c = 3.33 \cdot 10^4$, $Re_c = 6.67 \cdot 10^4$ and $Re_c = O(10^5)$.

In Figure 13, it was shown that some spectral density peaks appear outside of the natural frequency range of the system plate-scale for some tests ($f_{1st} = 28.25\ Hz$), and a power spectral density increase tendency especially for the low frequency components of the signal. This result is more pronounced for the higher Reynolds numbers.

In order to characterize these spectral density local peaks that appeared out of the natural frequency range, a new signal filtering was developed by a low-pass 10 Hz filter. Therefore, the components of longer period were isolated for each AoA and Reynolds number. It is possible that this sinusoidal temporal component of the measured force was due to the random fluctuation phenomenon of the wing tip vortex centroid position in the field close to the trailing edge (vortex meandering), this center fluctuation path has been characterized using flow visualizations for the same airfoil Del Pino et al. (2011).

In Figure 15 is shown the spectral energy of the filtered net force signal ($f \leq 10\ Hz$), normalized by the maximum spectral energy for each AoA. To improve the data observation, frequencies were plotted in

logarithmic scale. It can be observed that normalized energy peaks existed for frequencies lower than 0.2 Hz for all Reynolds numbers and dominated the dynamic response of the wing at low frequencies, especially for $Re_c = O(10^4)$. However, these peaks disappeared for small AoA ($0^o \leq \alpha \leq 8^o$) as Re_c increased over 10^5 due to other higher frequencies became more energetic. For AoA above 8^o, the dynamic response of the wing was again dominated by frequencies lower than 0.2 Hz for the higher Reynolds numbers.

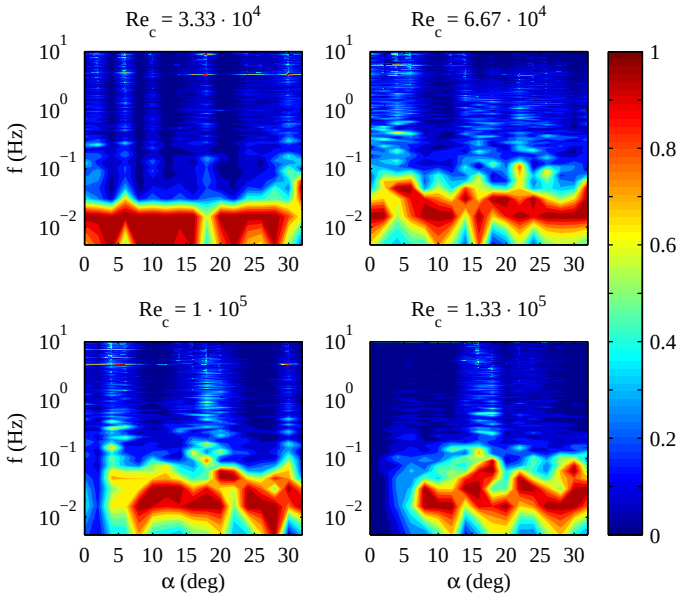

Figure 15: Normalized PSD of the net force signal for all Re_c cases at low frequencies.

This value of the most energetic frequency is in agreement with the experimental results reported in Del Pino et al. (2011)). In this work a vortex centroid position variation frequency at the perpendicular plane to the flow direction lower than 0.2 Hz was found for x/c ranging from 0 to 4 (near field) and $22504 \leq Re_c \leq 41874$. Roy and Leweke (2008) obtained, for the same phenomenon and using PIV, values for the fundamental frequency of the vortex center variation slightly less than 1 Hz, for a plane sited at $x/c = 11.2$ (far field) and $Re_c = O(10^6)$. Obviously, the observed low-frequency net force peaks on the wing could be related to this spatial fluctuation of the tip-vortex center. If tip-vortex meandering affects the aerodynamic forces on the wing, it can be inferred that the fundamental frequencies of this phenomenon in the near field to the trailing edge of the wing are more significant than the fundamental frequencies in the far-field region.

Finally, frequency temporal variations in the wing force fluctuations were also reviewed. On purpose, the temporary net force signal was fragmented by ten rectangular adjacent windows that cover 2^{13} sample points each, so they could detect up to 3 cycles of 0.09 Hz. A tapered frame with the *tanh* function is applied to each window in order to get the periodicity conditions at the window boundaries. Each window was analyzed using the *Matlab* FFT function. Small temporal variations in the spectral energy level exist for some frequencies but

the dominant frequencies are maintained throughout the time in each test, for all cases studied.

3.4. Fundamental vibration frequencies

As it was mentioned below, local energy peaks exist for frequencies corresponding to the first natural vibration frequency of the wing-scale system ($f_{1st} = 28.25\ Hz$, $f_{2nd} = 43.50\ Hz$) and to the main frequency of spatial variation of the tip-vortex center ($f \leq 0.2\ Hz$) in all tested Re_c. However, it can be observed (Figures 16, 17, 18 and 19) that, the spectral energy involved in the first natural frequency remains approximately constant with all angles of attack tested. However, the spectral energy peaks at frecuencies below $0.2\ Hz$ disappear for small angles of attack.

For the two lowest Reynolds numbers (Figures from 16 and 17), several energetic frecuencies exists near the first two natural frequencies f_{1st} and f_{2nd}. For the lowest Re_c, spectral energy peaks appear at frequencies $32\ Hz$ and $30\ Hz$, especially for small AoA. As the AoA grew above the stall angle, these frequencies lost some energy as the first two natural frequencies increase their energy. For both Reynolds numbers, local spectral energy peaks also appeared in the frequency range from $16\ Hz$ to $23\ Hz$, although the energy involved in these frequencies were much smaller than the spectral density corresponding to the first two natural frequencies. For $Re_c = 3.33 \cdot 10^4$, the energy at the frequency $f_{2nd} = 43.5\ Hz$ increased greatly for angles above the stall one and dominated even on the dynamic response of the wing. This frequency also appeared at $Re_c = 6.67 \cdot 10^4$, but with much lower energy. In addition, for $Re_c = 6.67 \cdot 10^4$ energetic frequencies occurred between $40\ Hz$ and $70\ Hz$.

For $Re_c = 1 \cdot 10^5$ (Figure 18), energetic frequencies appeared above $80\ Hz$ and the distortion around the first two natural frequencies disappeared almost completely. This fact also occurred for $Re_c = 1.33 \cdot 10^5$ (Figure 19), where there was a frequency of high energy at $116\ Hz$ approximately. The highest the Re_c was, the most dominant were the two first natural frequencies of wing-scale system on the dynamic response. However, the most energetic frequency for $Re_c = 1 \cdot 10^5$ corresponded to f_{2nd} again, especially for AoA $\alpha \geq 20^o$. For $Re_c = 1.33 \cdot 10^5$, f_{1st} was the most dominant.

It is possible to consider that spectral energy peaks, outside the range of the first two natural frequency and the fundamental frequency of the tip-vortex meandering phenomena, were due to the flow regime on the suction surface and the resulting interaction between vortex shedding in the wake and tip-vortex. It was also appreciated that these frequencies were increased as the Re_c. This fact is in agreement with previous works in this field [Lee and Huang (1998); Huang and Lin (1995) and Calderon et al. (2010)]. These works suggested that vortex shedding frequency in the wake increased with Re_c and decreased with AoA. In the same direction, Rojratsirikul et al. (2011) suggested that, for Reynolds numbers of the same order of magnitude to those studied in this paper, the wing aspect ratio had a limited influence on the vortex shedding frequency in the wake.

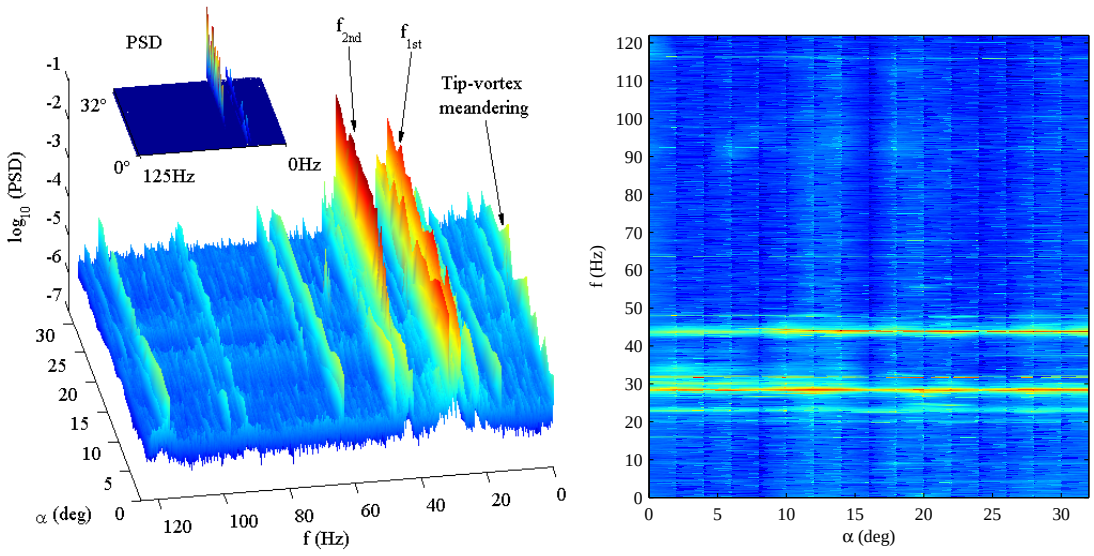

(a) (b)

Figure 16: Spectral density 3D (a) and 2D (b) mapping for $Re_c = 3.33 \cdot 10^4$ and angles of attack between 0^o to 32^o.

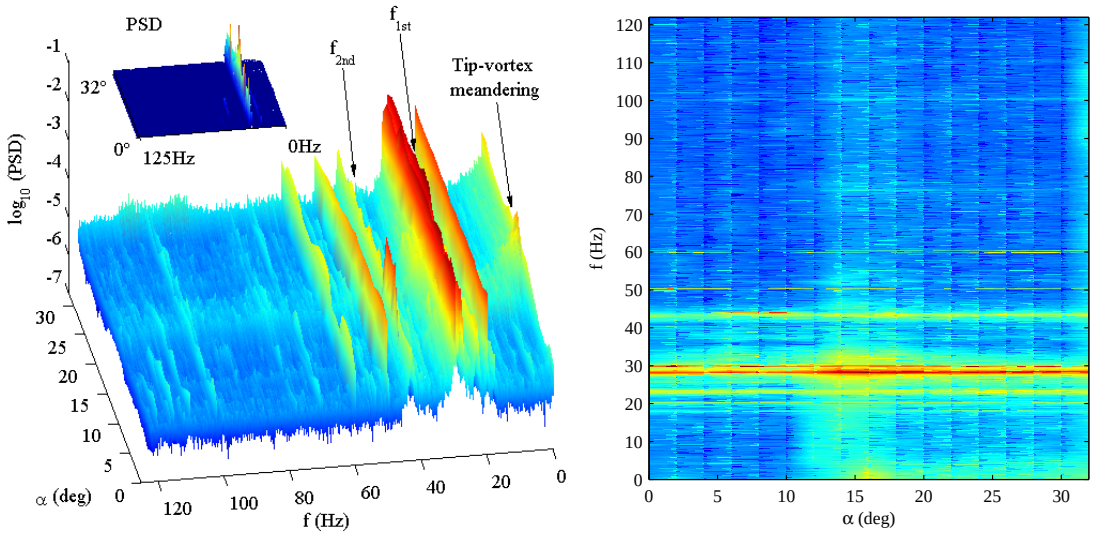

(a) (b)

Figure 17: Spectral density 3D (a) and 2D (b) mapping for $Re_c = 6.67 \cdot 10^4$ and angles of attack between 0^o to 32^o.

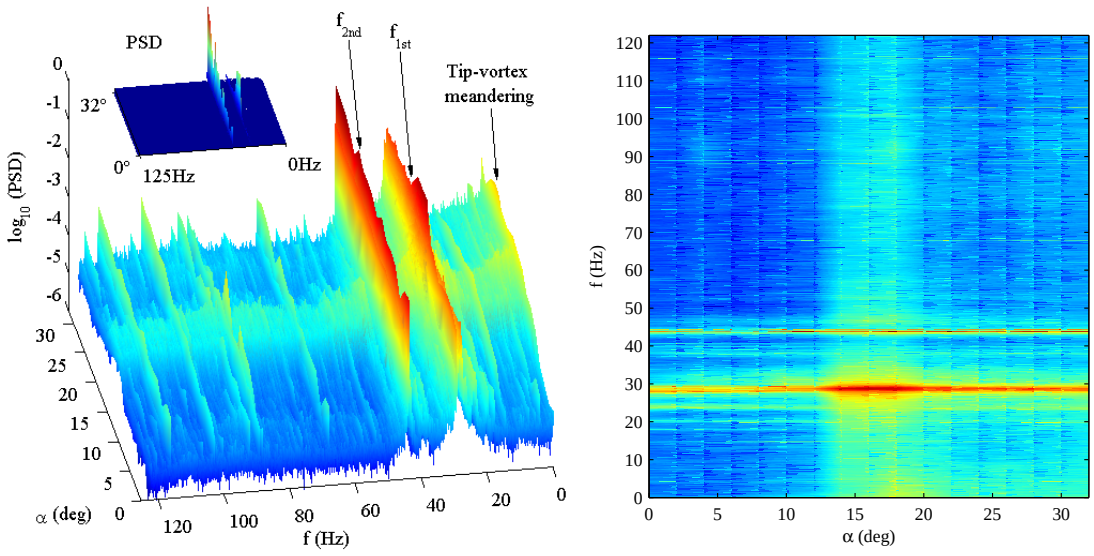

(a) (b)

Figure 18: Spectral density 3D (a) and 2D (b) mapping for $Re_c = 1 \cdot 10^5$ and angles of attack between 0^o to 32^o.

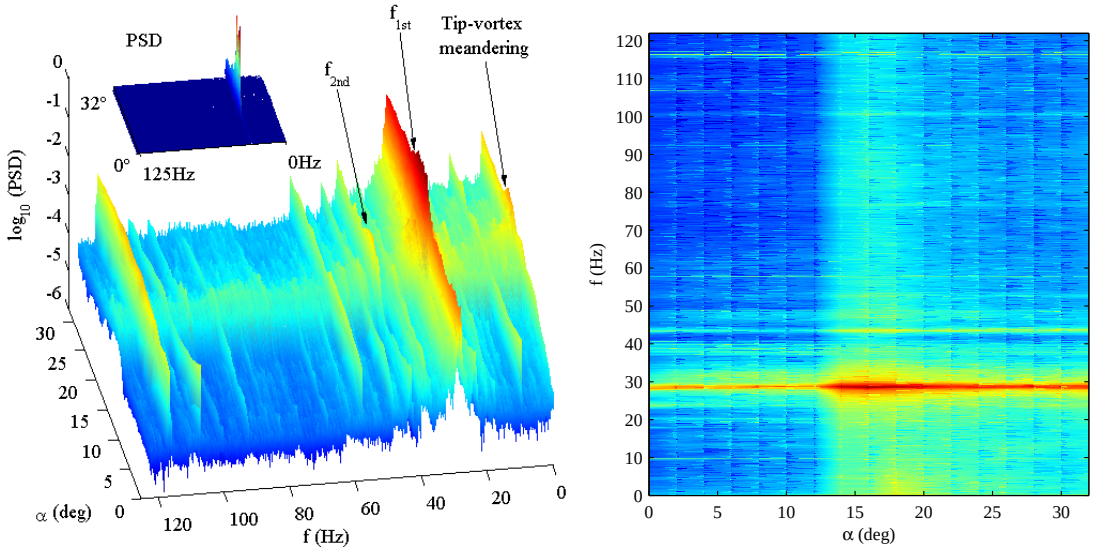

(a) (b)

Figure 19: Spectral density 3D (a) and 2D (b) mapping for $Re_c = 1.33 \cdot 10^5$ and angles of attack between 0^o to 32^o.

4. Conclusions

The dynamic response of a low aspect ratio airfoil NACA0012 at low-to-moderate Reynold numbers has been characterized by a precision force sensor. C_D, C_L and PSD are the main parameters that have been calculated from the force experimental data. Wing Tip Vortex generation and low aspect ratio ($AR = 2$) are the main causes of the lift force reduction respect to the NACA 0012 2D infinite profile. This reduction is almost 40% in all Reynolds numbers tested. The C_{Lmax} is slightly less than 0.6, with an increasing lift curve slope for zero AoA when the free stream velocity is also increased. The stall angle is about $12^o - 14^o$ and there is a minor increasing when the free stream velocity is also increased.

An universal fitting for the slopes of the lift coefficients curves $\Delta C_L/\Delta\alpha$ namely β_{L1} and β_{L2} and for any AR has been proposed. $\beta_{L1} \cdot AR^{-0.5}$ was strongly dependent on Re_c for $Re_c \leq 1 \cdot 10^5$, but for higher Re_c, the $\beta_{L1} \cdot AR^{-0.5}$ tendency changed to remain almost constant with Re_c variation. $\beta_{L2} \cdot AR^{-0.5}$ is almost independent of Re_c.

In the same way, this edge effect generates an induced drag force that enlarge wing drag coefficient 6 times over the theoretical 2D reference. The minimum drag coefficient is obtained for $\alpha = 0^o$ AoA and its value is between 0.053 and 0.072. The relation between C_{Dmin} and Re_c could be experimentally adjusted for any AR by the expression $CD_{min} = 2/AR \cdot Re_c^{-0.25}$. In addition, we have proposed a C_{Lmax}/C_{Dmin} correlation for any AR: $C_{Lmax}/C_{Dmin} = 0.27 \cdot AR \cdot Re_c^{0.25}$

By analyzing the time series of the variation of the force on the wing model in the frequency domain, it was found that two frequencies of 28.25 Hz and 43.50 Hz involved a high energy, regardless of AoA and Re_c. These independent and dominant frequencies were obviously due to a mechanical response to the excitation of the wing. The two first natural frequencies of the wing-balance system (f_{1st} and f_{2nd}), which had been experimentally determined by ten impacts tests. Likewise, this data was compared with experimental and theoretical results obtained for a rectangular flat plate cantilever, mechanically equivalent to our wing-scale model, and all first natural frequency values were mainly in agreement.

Spectral density local peaks were found for frequencies lower than 0.2 Hz in all chord Reynolds numbers cases tested, especially for angles of attack above the stall one. These components may be due to a phenomenon consisting in the spatial centroid variation of the vortex generated by the wing tip in the near field to the trailing edge of the wing, called tip-vortex meandering.

Other Spectral density local peaks were found for frequencies $O(10^1 - 10^2)$ Hz. On the one hand, it was also appreciated that these local peak frequencies were increased as the Re_c. It is possible to relate the spectral energy peaks to the formation and emission of coherent turbulent structures on the suction surface, and the resulting interaction between vortex shedding and tip-vortex in the wake. On the other hand, the vibration intensity increased greatly for AoA slightly higher than the stall one ($12^o \leq \alpha \leq 20^o$), especially if Re_c increases. This fact is related to buble bursting and turbulent separation.

5. Acknowledgement

This work has been supported by Grant Proyecto de Excelencia de la Junta de Andaluca number P11-TEP7776.

References

Abbott, I.H., von Doenhoff, A.E., 1959. Theory of wing sections. Dover Publications, Inc., New York.

Calderon, D.E., Wang, Z., Gursul, I., 2010. Lift enhancement of a rectangular wing undergoing a small amplitude plunging motion. 48th AIAA Aerospace Sciences Meeting, Orlando (USA). AIAA-2010-386 .

Dalley, J.W., Ripperger, E.A., 1954. Experimental values of natural frequencies for skew and rectangular cantilever plates, Def. Res. Lab. Rept. DRL-231, CF-1359, University of Texas (USA).

Del Pino, C., Lopez-Alonso, J.M., Parras, L., Fernndez-Feria, R., 2011. Dynamics of the wing-tip cortex in the near field of a naca 0012 airfoil. The Aeronautical Journal 115.

Gerakopulos, R.J., 2011. Investigating flow over an airfoil al low reynolds numbers using novel time-resolved surface pressure measurements, Doctoral Tesis, University of Waterloo, Ontario (Canada).

Gad-el Hak, M., 1990. Control of low-speed airfoil aerodynamics. AIAA Journal 28, 1537–1552.

Huang, R.F., Lee, H.W., 1999. Effects of freestream turbulence on wing-surface flow and aerodynamic performance. Journal of Aircraft 36, 965–972.

Huang, R.F., Lee, H.W., 2000. Turbulence effects on frequency characteristics of unsteady motions in wake of wing. AIAA Journal 38, 85–93.

Huang, R.F., Lin, C., 1995. Vortex shedding and shear-layer instability of wing at low-reynolds numbers. AIAA Journal 33, 1398–1403.

Keuthe, A.M., Chow, C.Y., 1997. Foundations of Aerodynamics: Bases of aerodynamic design. Wiley, New York. 5th ed. edition.

Kim, D.H., Chang, J.W., 2013. Low-reynolds-number effect on the aerodynamic characteristics of a pitching naca 0012 airfoil. Aerospace Science and Technology in press.

Kline, S.J., McClintock, F.A., 1953. Describing uncertainties in single-sample experiments. Mechanical Engineering 75, 3–8.

Laitone, E.V., 1997. Wind tunnel test of wings al reynolds number bellow 70000. Experiments in Fluids 23, 405–409.

Lee, H.W., Huang, R.F., 1998. Frequency selection of wake flow behing a naca 0012 wing. Journal of Marine Science and Technology 6, 29–37.

McArthur, J., 2008. Aerodynamics of wings at low reynolds numbers: boundary layer separation and reattachment .

Mueller, T.J., 1985. Low reynolds number vehicles, AGARD-AG-288.

Mueller, T.J., 1999. Aerodynamics measurement at low reynolds numbers for fixed wing micro-air vehicles, Hessert Centre for Aerospacial Research, Department of Aerospace and Mechanical Engineering, University of Notre Dame, Indiana (USA).

Mueller, T.J., Torres, G.E., 2001. Aerodynamics of low aspect ratio wings at low reynolds numbers with application to micro-air vehicles design an optimization, Hessert Centre for Aerospacial Research, Department of Aerospace and Mechanical Engineering, University of Notre Dame, Indiana (USA).

Ngo, H.T., Barlow, L.E., 2002. Lifting surface with active variable tip member and method for influencing lifting surface behavior therewith, United State Patent No. US 6.394.397 B1.

Poirel, D., Harris, Y., Benaissa, A., 2008. Self-sustained aeroelastic oscillations of a naca0012 airfoil at low-to-moderate reynolds numbers. Journal of Fluids and Structures 24, 700–719.

Poirel, D., Yuan, W., 2010. Aerodynamics of laminar separation flutter at a transitional reynolds number. Journal of Fluids and Structures 26, 1174–1194.

Rojratsirikul, P., Genc, M.S., Wang, Z., Gursul, I., 2011. Flow-induced vibrations of low aspect ratio rectangular membrane wings. Journal of Fluids and Structures 27, 1296–1309.

Rojratsirikul, P., Wang, Z., Gursul, I., 2010. Effect of pre-strain and excess length on unsteady fluidstructure interactions of membrane airfoils. Journal of Fluids and Structures 26, 359–376.

Roy, C., Leweke, T., 2008. Experiments on vortex meandering. Technical Report 111-4 STREP, Fundamental Research on Aircraf Wake Phenomena CNRS-IRPHE .

Sheldahl, R.E., Klimas, P.C., 1981. Aerodynamics characteristics of seven symmetrical airfoil sections through 180 degree angle attack for use in aerodynamics analysis of vertical axis wind turbines, Sandia National Laboratories, Albuquerque (USA), SAND80-2114.

Warburton, G.B., 1954. The vibration of rectangular plates. Proc. Inst. Mech. Eng. 168, 371–384.

Yarusevych, S., Sullivan, P.E., Kawalls, J.G., 2009. On vortex shedding from an airfoil in low-reynolds-number flows. Journal of Fluid Mechanics 632, 245–271.

Yen, S.C., Huang, L.C., 2009. Flow patterns and aerodynamics performance of unswept and swept-back wings. Journal of Fluids Engineering 131, 111101–1–10.

Yen, S.C., Huang, L.C., 2011. Reynolds number effects on flow characteristics and aerodynamic performances of a swept-back wing. Aerospace Science and Technology 15, 155–164.

Figure captions

Figure 1: NACA 0012 model mounted in the wind tunnel.

Figure 2: Precision 3D scale and automatic system of rotation.

Figure 3: C_D vs α with a detail for high Reynolds numbers, together with those reported by Ngo and Barlow (2002), Mueller and Torres (2001) and Sheldahl and Klimas (1981).

Figure 4: (a) C_{Dmin} vs Re_c for $3.33 \cdot 10^4 \leq Re_c \leq 1.33 \cdot 10^5$ and $AR = 2$ compared with the results of Ngo and Barlow (2002), Yen and Huang (2009), Laitone (1997) and Sheldahl and Klimas (1981). (b) $CD_{min} \cdot AR$ vs Re_c for the universal fitting law $CD_{min} = 2/AR \cdot Re_c^{-0.25}$.

Figure 5: C_L vs α with a detail for high Reynolds numbers, together with those reported by Ngo and Barlow (2002), Mueller and Torres (2001) and Sheldahl and Klimas (1981). Detail: β_{L1} and β_{L2} for higher Reynolds numbers compared to the result from Prandtls lifting line theory for symmetric, rectangular wing with no twist and finite span Keuthe and Chow (1997).

Figure 6: C_L vs α for $Re_c = 3.33 \cdot 10^4$ and $Re_c = 6.67 \cdot 10^4$ with AoA values lower than the stall angle ($AR = 2$), together with Laitone's data ($AR = 6$, $I = 0.02\%$).

Figure 7: (a) Universal fitting for $\beta_{L1} \cdot AR^{-0.5}$ vs Re_c for $3.33 \cdot 10^4 \leq Re_c \leq 1.33 \cdot 10^5$ and $AR = 2$ compared with the results of Ngo and Barlow (2002), Yen and Huang (2009), Laitone (1997) and Sheldahl and Klimas (1981). (b) Universal fitting for $\beta_{L2} \cdot AR^{-0.5}$ vs Re_c. (c) C_{Lmax} vs Re_c for $3.33 \cdot 10^4 \leq Re_c \leq 1.33 \cdot 10^5$ and $AR = 2$ compared with the results of Ngo and Barlow (2002), Yen and Huang (2009) and Laitone (1997).

Figure 8: C_L/C_D vs α for all Reynolds numbers tested.

Figure 9: (a) C_{Lmax}/C_{Dmin} vs Re_c for $3.33 \cdot 10^4 \leq Re_c \leq 1.33 \cdot 10^5$ and $AR = 2$ compared with the results of Ngo and Barlow (2002), Yen and Huang (2009), Laitone (1997) and Sheldahl and Klimas (1981). (b) $C_{Lmax}/C_{Dmin} \cdot AR^{-1}$ versus Re_c for the universal fitting law: $C_{Lmax}/C_{Dmin} = 0.27 \cdot AR \cdot Re_c^{0.25}$.

Figure 10: (a) C_D y C_L deviations for $Re_c = 1.33 \cdot 10^5$ and (b) absolute deviations of the coefficients for all AoA and Reynolds numbers tested.

Figure 11: Net force vs time and power spectral density (PSD) for three impacts at the free end wing. The main vibration frequency of the system was 28.25 Hz in all impact tests.

Figure 12: Net force vs time and power spectral density (PSD) for three impacts at the cilindrical base. The second main vibration frequency of the system was 43.50 Hz in all impact tests.

Figure 13: PSD of the net force signal for (a) $Re_c = 3.33 \cdot 10^4$, (b) $Re_c = 6.67 \cdot 10^4$, (c) $Re_c = 1 \cdot 10^5$ and (d) $Re_c = 1.33 \cdot 10^5$, and angles of attack between 0^0 to 30^o.

Figure 14: PSD of the net force signal for all Re_c cases and angles of attack $\alpha = 6^o$, $\alpha = 18^o$ and $\alpha = 30^o$.

Figure 15: Normalized PSD of the net force signal for all Re_c cases at low frequencies.

Figure 16: Spectral density 3D (a) and 2D (b) mapping for $Re_c = 3.33 \cdot 10^4$ and angles of attack between 0^o to 32^o.

Figure 17: Spectral density 3D (a) and 2D (b) mapping for $Re_c = 6.67 \cdot 10^4$ and angles of attack between 0^o to 32^o.

Figure 18: Spectral density 3D (a) and 2D (b) mapping for $Re_c = 1 \cdot 10^5$ and angles of attack between 0^o to 32^o.

Figure 19: Spectral density 3D (a) and 2D (b) mapping for $Re_c = 1.33 \cdot 10^5$ and angles of attack between 0^o to 32^o.

Tables

$\%P$	$U_\infty\ [m/s]$	$\delta U_\infty [m/s]$	Re_c	$I[\%]$
0.68	5	± 0.06	$3.33 \cdot 10^4$	1.2
11.25	10	± 0.12	$6.67 \cdot 10^4$	1.2
21.43	15	± 0.16	$1 \cdot 10^5$	1.1
30.56	20	± 0.47	$1.33 \cdot 10^5$	2.3

Table 1: Wind velocities and chord Reynolds numbers tested.

Re_c	$\%\ Error\ C_D$	$\%\ Error\ C_L$
$3.33 \cdot 10^4$	± 4.0	± 3.0
$6.67 \cdot 10^4$	± 6.0	± 4.5
$1 \cdot 10^5$	± 6.5	± 4.5
$1.33 \cdot 10^5$	± 5.5	± 4.0

Table 2: Estimated maximum errors in % of the coefficients C_D and C_L.

<table>
<tr><th></th><th colspan="2">Low Reynolds numbers</th><th>High Reynolds numbers</th></tr>
<tr><td></td><td colspan="3">$--\longrightarrow$ PSD increases with Re_c increase $\longrightarrow ++$</td></tr>
<tr><td></td><td>$Re_c = 3.33 \cdot 10^4$</td><td>$Re_c = 6.67 \cdot 10^4$</td><td>$Re_c = O(10^5)$</td></tr>
<tr><td rowspan="2">$\alpha \leq \alpha_{stall}$</td><td colspan="2">PSD remains constant

Laminar Separation regime: f_o and f_s does not depend on AoA,
Separation Bubble regime: f_o increases slightly and f_s decreases with AoA increase</td><td>PSD increases slightly

Separation Bubble regime: f_o increases slightly and f_s decreases with AoA increase</td></tr>
<tr><td colspan="3">$--\longrightarrow$ f_o and f_s increase with Re_c increase $\longrightarrow ++$</td></tr>
<tr><td rowspan="2">$\alpha_{stall} \leq \alpha \leq 20^o$</td><td>PSD remains constant</td><td>PSD increases sharply, especially at low frequencies</td><td>PSD increases sharply at all frequencies</td></tr>
<tr><td colspan="3">Bubble Burst and Turbulent Separation regime: sharp drop in f_o
$--\longrightarrow$ The frequency drop is more pronounced for higher Re_c $\longrightarrow ++$</td></tr>
<tr><td rowspan="2">$\alpha > 20^o$</td><td>PSD remains constant</td><td>PSD decreases progressively, especially at low frequencies</td><td>PSD decreases progressively at all frequencies</td></tr>
<tr><td colspan="3">3D Flow regime: f_s decreases slightly with AoA increase
$--\longrightarrow$ f_s increases slightly with Re_c increase $\longrightarrow ++$</td></tr>
</table>

Table 3: PSD changes with AoA and Re_c, together with shear-layer regimes and shedding vortex frequency variations.